Corrosion Science 190 (2021) 109702

Contents lists available at ScienceDirect

Corrosion Science

journal homepage: www.elsevier.com/locate/corsci

Inhibition of metal dusting corrosion on Fe-based alloy by combined near surface severe plastic deformation (NS-SPD) and thermochemical treatment

Xiaoyang Guo [a,1], Per Erik Vullum [b,c], Hilde J. Venvik [a,*]

[a] Department of Chemical Engineering, NTNU - Norwegian University of Science and Technology, Trondheim, NO–7491, Norway
[b] SINTEF Industry, Trondheim, NO–7465, Norway
[c] Department of Physics, NTNU - Norwegian University of Science and Technology, Trondheim, NO–7491, Norway

ARTICLE INFO

Keywords:
Metal dusting corrosion
Near surface severe plastic deformation
Grain refinement
TEM
Raman spectroscopy

ABSTRACT

Combined NS-SPD and thermochemical treatment has been used to improve the metal dusting corrosion resistance of Incoloy 800. After testing under infinite carbon activity for 20−100 h, carbon was not found in the NS-SPD region while corrosion products formed in the non-NS-SPD region. The improved resistance is a result of the NS-SPD yielding a high density of defects in the deformation zone that developed into an ultra-fine-grained structure near the surface during the subsequent thermochemical treatment. These microstructural changes increase the effective diffusion coefficient for Cr in the alloy, hence promoting the formation of a highly protective oxide scale.

1. Introduction

The stability of metallic materials is critical to their sustainable use in a wide range of applications. Oxide scale grown or formed on the alloy surface provides an effective and relatively inexpensive way to protect the metallic matrix against a range of high-temperature degradation phenomena [1,2]. The properties of the oxide scale affect the corrosion resistance of the alloy, thereby determining e.g. the service life of process equipment. Among the materials stability challenges, so-called metal dusting corrosion is a critical issue in a range of chemical industries. This is a high-temperature degradation phenomenon affecting Fe- and Ni-based alloys when exposed to highly carburizing conditions (carbon activity $a_c > 1$) at elevated temperature ($T > 400$ °C) [3–6]. The interaction with carbon species in the process gas, typically CO, CO_2, CH_4, C_2H_4, etc., leads to the formation of unwanted carbon on the surface, and subsequent ingress of carbon into the alloy, which then gradually disintegrates into a powder mixture of metallic, carbide and carbonaceous dusts. Metal dusting corrosion has been studied for decades, and several mechanisms for this phenomenon have been proposed [4,7–13]. It starts due to the thermodynamic driving force of the process gas ($a_c > 1$) but is strongly controlled by the kinetics of carbon formation. The industrial process conditions cause transfer of carbon to the alloy surface by one or more of the CO reduction, Boudouard, and alkane thermal cracking reactions [14]. Fe, Co, and Ni, as well as their alloys, are known to catalyze these reactions, while simultaneously being - at least Fe and Ni - among the most important components of alloys applicable at high temperature. For Fe-based alloys [4,5,14], the corrosion proceeds by the formation of Fe_3C or Fe_5C_2 carbides, and the associated volume expansion creates additional defects in the alloy surface layer [15,16]. Carbon then precipitates at defects, and accumulation of carbonaceous deposits separates the carbide particles from the metallic matrix to be transported away from the alloy surface to leave a pit.

Several aspects influence the selection of a metallic material for high-temperature applications, including mechanical and thermal properties, corrosion and erosion resistance, as well as cost. It is, however, difficult or even impossible to combine the different desired properties in one single material. In industry, different precautionary methods exist to suppress metal dusting corrosion. These include the use of inhibitors (e.g. H_2S and C_2S) to reduce the catalytic activity on the alloy surface, careful selection and adjustment of processing parameters (P, T, C), applying coatings or developing resistant oxide scales on the metal surface, as well as developing new alloys with better resistance. Each of these have challenges and/or cost associated, e.g. the inhibitors may be detrimental elsewhere in the process, parameter adjustment causes efficiency loss, coatings may crack and loose adherence and even

* Corresponding author.
E-mail address: hilde.j.venvik@ntnu.no (H.J. Venvik).
[1] Current affiliation: PRECOR AS, Utleirvegen 10, 7033 Trondheim, Norway

https://doi.org/10.1016/j.corsci.2021.109702
Received 9 April 2021; Received in revised form 5 July 2021; Accepted 17 July 2021
Available online 21 July 2021

compromise required functions such as heat transfer, and optimally designed materials may be prohibitively expensive and in limited supply. A protective surface layer different in structure and/or chemical composition and supplied by a surface treatment may thus be considered an optimum solution to obtain a performance compromise [17], and it is known from several investigations that metal dusting corrosion can be inhibited by dense and stable oxide scales [18–21].

In many industrial processes at elevated temperature, Fe- and Ni-based alloys are used with Cr as an advantageous secondary constituent. Cr can be preferentially oxidized to form slow-growing, well-adherent, and dense chromium oxide layers that have generally good corrosion resistance [22]. Incorporation of chromium (Cr) in the alloy to facilitate the formation of a Cr oxide at the surface is also being applied to prevent metal dusting since Cr_2O_3 does not catalyze the carbon formation and is known to remain stable in carbonaceous atmospheres down to very low oxygen partial pressure [23]. The presence of Al may correspondingly support the formation of a protective, thermodynamically stable, Al_2O_3 layer [24,25]. The diffusion of carbon atoms through Cr_2O_3 (and Al_2O_3) matrices is not facile [26]. Protective surface layers of Cr_2O_3 have hence demonstrated excellent performance in this respect [27,28]; provided a dense and defect-free oxide layer that prohibits access to the bulk matrix can be formed and maintained during industrial operation.

Chromium oxide adopts the structure of corundum, consisting of a hexagonal close-packed array of oxide anions with 2/3 of the octahedral sites occupied by chromium [29]. In addition to Cr_2O_3, oxidation of alloys may lead to formation of a range of spinels [30,31]. Some spinels are reported to have good metal dusting resistance, while others are unfavorable. A high Fe-content in the spinel has been reported to render the surface scale non-protective against metal dusting, due to high carbon diffusion rates through these spinels [32]. Manganese (Mn) constitutes a main alloying element in high-temperature alloys since it can stabilize the austenitic structure in the Fe-Ni-Cr alloy system. Mn is also known as an element that can diffuse to the surface [33]. The mobility of Mn in Cr_2O_3 [22] enables the formation of a $MnCr_2O_4$ spinel phase, and this spinel is established as a good protective scale [34–39]. Fe-based superalloy doped with other elements, e.g. yttrium, has also demonstrated anti-coking and anti-carburizing properties [40].

Any Cr_2O_3 oxide created on an alloy surface is not, however, generally able to protect the underlying matrix [41]. Common oxidation processes often yield oxide scales composed of two layers: an outer layer rich in Fe and an inner layer rich in Cr [30,42–44]. This outer oxide layer may be reduced under working conditions to form Fe particles that act as catalysts for carbon formation leading to metal dusting corrosion. Moreover, the integrity of the layer depends on its thickness and structure. The thickness should be large enough to shield the underlying matrix, but an increased thickness may eventually enhance the effects of incompatibility in thermal expansion between the two layers, which counteract the protective effect by inducing cracks and causing delamination. Likewise, the crystallites should have good adherence to each other and the metal so that pores for gas diffusion do not exist. Strategies applied to create a protective Cr-containing oxide that prevents contact between the carburizing atmosphere and the Ni and Fe contained in the alloy hence need to be optimized with respect to thickness, composition, and structure.

Various imperfections in a metal matrix (e.g. vacancies, dislocations and grain boundaries) can change the properties of an alloy to a large degree [45,46]. In particular, structural defects increase the effective diffusion coefficient of Cr in the alloy by introducing a higher density of rapid diffusion paths, hence promoting the formation of a Cr-rich oxide scale during oxidative treatment at elevated temperature. The diffusion of Cr in superalloy Incoloy 800 has been studied by A.R. Paul et al. with a serial sectioning technique using a radioactive tracer ^{51}Cr for the grain boundary and lattice diffusion [47]. They found that the activation energy for lattice diffusion is much higher than for grain boundary diffusion and that for small-grained specimens at temperature lower than ~700 °C, transport of chromium atoms mainly proceeded via the grain boundaries [47].

The defect structure and grain boundary density are generally determined by and can be manipulated during the alloy fabrication. Recently, the processing of metallic materials through the application of severe plastic deformation (SPD) has been intensively studied [48,49]. The SPD processing is able to refine the grain structure of metallic materials to sub-micrometer and nanometer ranges. However, special equipment and/or techniques together with large amounts of energy are needed for SPD processes to produce bulk, ultrafine-grained (UFG) materials [50]. Therefore, methods to modify the grain boundary and defect structure in the near surface region are being developed. Near surface severe plastic deformation (NS-SPD) or Surface severe plastic deformation (S^2PD) processes have been shown to introduce nanograins and grain size gradients into the surface region of metallic materials [51]. Materials treated by NS-SPD (or S^2PD) display a large number of structural defects, i.e., grain boundaries, dislocations, and triple points in the near surface region [52–54]. This leads to a significant increase in stored energy, which may increase the reactivity of the material and yield different effects on the corrosion behavior, depending upon the material-environment system [52,55,56]. In non-passivating electrolytes (e.g., H_2SO_4 and HCl), a nanocrystalline structure is reported to enhance the corrosion rate, whilst superior corrosion resistance is reported in passivating solutions (e.g., NaCl and NaOH) [55]. K. Bokati et al. [57] reported on the inhibition performance of sodium molybdate (SM) and 1H-benzotriazole (BTA) on low-carbon steel in artificial sea water. The NS-SPD promoted the adsorption of the corrosion inhibitors by creating a surface with a high density of preferential adsorption sites. Enhanced adsorption of molybdate ions and better stability of the protective layer formed on the surface by the sodium molybdate solution was obtained. B.T. Lu and co-workers studied the effect of cold work on the surface of UNS (unified numbering system) N08800 alloy in corroding environments using *in-situ* scanning electrochemical microscopy and reported the plastic deformation to increase the surface reactivity [58]. T. Wang et al. [59] reported the surface nanocrystallization of 1Cr18Ni9Ti stainless steel achieved by using high-energy shot peening to enhance the overall and local corrosion resistance of the steel in Cl^--containing solution. W. Zhao et al. [60] induced a surface plastic deformation layer on ultra-high strength steel by ultrasonic nanocrystal surface modification and nitriding. The enhanced surface roughness of the severe surface plastic deformation layer generated by the pre-treatment promoted the corrosion properties of the steel, but the best corrosion resistance was obtained in combination with nitriding, found to result from the generation of a thicker nitride layer and an increase in nitrogen concentration.

In materials treated by NS-SPD (or S^2PD), the diffusivity of alloying elements is generally significantly higher than in conventional coarse grained materials as a result of the considerable higher fraction of structural defects [61]. L. Tan et al. [62] investigated the effect of shot-peening on the oxidation behavior of alloy 800H exposed to supercritical water and cyclic oxidation. The processing created a ~70 μm deformation zone composed of an ultrafine-grained region near the surface and a transition below. An increased population of grain boundaries was found to assist in the formation of Cr-rich oxides. The surface severe plastic deformation processing was also shown to mitigate oxide exfoliation on the alloy 800H surface [62]. C. Chen et al. [63] applied a combination of Al diffusion treatment and surface nanocrystallization to demonstrate improved corrosion resistance of non-passive carbon steel. An improvement in corrosion resistance because of the enhanced diffusion of chromium was also found by X. Ren et al. [64], who investigated the effects of grain refinement by shot peening on the corrosion behavior of three ferritic-martensitic steels, HT9, T91, and NF616, and two binary model alloys Fe-15 %Cr and Fe-18 %Cr in supercritical water. S. Bahl et al. [65] subjected 316L stainless steel to surface mechanical attrition treatment to generate a nanocrystalline surface, which led to an increase in the corrosion fatigue

strength. This was attributed to higher strength of the nanocrystalline layer, compressive residual stresses, a thicker oxide layer, and enhanced resistance to intergranular corrosion due to the nanoscale microstructure. H.S. Arora et al. [66] utilized submerged friction stir processing to develop tailored microstructures in stainless steel, and higher corrosion resistance in standalone corrosion testing was attributed to higher pitting resistance and faster passivation kinetics of the fine-grained structure.

Several studies have been conducted on the surface pretreatment of alloys prior to exposure to carburizing conditions in an effort to protect against metal dusting. The results have shown that a positive effect of grinding, as compared to electropolishing [27,67], pickling [68] and chemical etching [18,27,69–71] can be attributed to the deformation layer on the surface providing rapid diffusion paths for chromium to form a chromia scale on the surface. Wen-Ta Tsai and co-workers studied the effect of surface treatment on the 304 L stainless steel exposed to a mixed gas of $CO/CO_2 = 100/1$ in the range 500–700 ℃ using thermogravimetric analyses [72]. Their results showed that the formation of graphite and nano-sized carbon filaments was affected by the surface pre-treatment applied to the stainless steel. The severe surface plastic deformation yielded facile diffusion paths for Cr that favored the formation of a protective Cr rich oxide. Enhanced carbon deposition but significant resistance to metal dusting corrosion was reported. Chun et al. [73] applied surface grinding of 304 stainless steel and found that the formation of a Cr-rich spinel oxide film is favored by a coarser alloy surface finish thereby providing initial protection from carbon ingress at high temperature corrosion. However, the spinel formed contained a significant amount of Fe and was hence believed to remain stable only for a limited period [73]. Voisey et al. [19] applied laser surface melting to the surface of alloy 800H to create a refined microstructure that increased the effective diffusion coefficient for Cr in the alloy. The resulting oxide scale contained, however, Fe spinel in addition to Cr_2O_3, and further treatment was therefore required to maintain a significantly improved metal dusting resistance. A. Vernouillet et al. [74] also applied laser beam melting (LBM) on the surface of Inconel 625 to enhance the resistance to metal dusting. Non ground LBM samples show higher mass variations than ground samples as a result of a higher dislocation density below the surface due to grinding.

In the present study, the near surface severe plastic deformation (NS-SPD) was applied to pre-polished Fe-based superalloy (Incoloy 800) coupons to obtain a gradient structure, i.e. from ultrafine grains at and near the surface to the coarse, original grain structure (~30−70 μm) in the bulk of the alloy. The coupons were thereafter subjected to consecutive thermochemical treatments at elevated temperature to form an oxide scale on the alloy surface. To test the resulting scale, the alloy coupons were exposed to a gas atmosphere with infinite carbon activity ($a_c >> 1$) at 550 °C for up to 100 h. Detailed characterization after each step was performed in order to establish a relationship between the structure and composition of the alloy surface and its propensity to solid carbon formation.

2. Experimental procedure

Incoloy 800 coupons with dimension 15 mm × 8 mm × 0.5 mm and 30−70 μm average grain size were prepared to investigate the method. All the coupons were first ground with SiC papers up to P2400 (10 μm) and finally polished with 1 μm diamond dust to yield a mirror finish. The samples were ultrasonically cleaned in hexane prior to the NS-SPD treatment. A tweezer was used manually at ambient temperature to plastically deform part of the near surface region of the alloy coupons (NS-SPD), and the resulting samples were thoroughly cleaned with ethanol and acetone before subjected to oxidization and carburization as described below.

The two-step thermochemical treatment was conducted in a laboratory experimental setup with a vertical tube reactor enclosed in a furnace. The alloy coupons were hung inside the steel tube, which has its internal wall plated with gold to mitigate the effect of metal dusting corrosion on the reactor [75]. The first step involved ramping the temperature by 10 °C/min to 540 °C in 10 % steam in Ar at 1 bar, and then maintaining this temperature for 6 h. In the second step, the temperature was increased to 750 °C, a mixture of H_2 (25 %), CO (20 %), CO_2 (15 %), H_2O (10 %) and Ar (30 %) was introduced, and the pressure was increased to 20 bar. The second thermochemical treatment step lasted altogether 20 h. To test the resulting oxide layer, a carburizing gas with 10 % CO in Ar, representing infinite carbon activity ($a_c >> 1$), was fed at 100 Nml/min total flow rate for up to 100 h.

Samples were characterized for each step of the NS-SPD, thermochemical treatment and exposure to the carburizing gas. Scanning electron microscopy (SEM), Raman spectroscopy and transmission electron microscopy (TEM) were the techniques employed to obtain information on the samples' chemistry and microstructure. The Zeiss Ultra 55 LE thermal field emission gun scanning electron microscope (FEG-SEM) was operated at 10 kV. The Horiba Jobin Yvon LabRAM HR800 spectrometer, using a 633 nm He-Ne laser emission line, was focussed on the sample using a motorized x–y stage 50 × long working distance (LWD) objective and 8 mW laser output power. The Raman spectra were recorded by continuous scanning in the range 300-3000 cm^{-1}, taking all spectra at three different locations on the sample (spot diameter ~1.5 μm) to ensure representative surface characteristics. The Raman line scan spectra was recorded across an NS-SPD area after alloy sample subjected to carburizing exposure for 20 h and ultrasonic agitation in acetone for 30 min. Agitation in acetone was needed to remove loosely adhered corrosion products as well as to facilitate the focussing on the alloy surface. Thin, cross-section lamellae for TEM were prepared from selected samples by focused ion beam (FIB) sputtering under SEM. The methodology and instrumentation to prepare the thin lamellae and the following characterization by TEM have been described in detail elsewhere [76]. It should be noted that carbon or platinum protection layers (taking care to avoid ion-beam induced surface damage) were deposited on the selected regions prior to the milling. The bulk composition of the fresh Incoloy 800 sample was also obtained by electron microprobe analysis (EMPA) via wavelength-dispersive X-ray spectroscopy (WDS) (Table 1), and found to be in agreement with the specifications of this superalloy [42].

3. Results

The development in overall surface characteristics of polished Incoloy 800 samples with the right side treated by NS-SPD is illustrated by the SEM micrographs in Fig. 1 (a–d), for each step of the NS-SPD, pre-oxidation and metal dusting corrosion testing. SEM images of the two TEM lamellae prepared by FIB from the alloy samples before and after corrosion testing are given in Fig. 1 (e–f). These illustrate the cross-section preparation and will be discussed in further detail below.

Fig. 1 (a) shows that the NS-SPD region is slightly pressed down with marks from the scratching. In the middle of the imaged region, a Pt layer has been deposited *in-situ* to protect the surface during subsequent ion milling to prepare the TEM lamella. Both the polished and the NS-SPD regions are included in the area of interest covered by the coating, thus also the transition region between these. The surface of Incoloy 800 changes upon oxidation in 10 % steam at 540 °C for 6 h, as shown in Fig. 1 (b). Compared to the polished sample in Fig. 1 (a), the surface is rougher, especially in the NS-SPD region. A protection layer of C was deposited on the alloy surface before ion milling and can be observed in the center of the image. An SEM image of the alloy sample after the second step of the thermochemical treatment, i.e. 20 bar syngas exposure at 750 °C for 20 h is displayed in Fig. 1 (c). The polished and NS-SPD regions now show unambiguous differences. Both are completely covered by crystal-like features that could not be observed before the second step of the thermal treatment. The surface crystallites in the polished region are considerably larger than those in the NS-SPD region. Hence, the surface has become even rougher after the second step, but in

Table 1
Elements present in the fresh Incoloy 800 sample, determined by EMPA/WDS.

Composition basis	Element percentage (%)								
	Fe	Ni	Cr	Mn	Al	Si	Ti	Cu	C
Avg. atomic	45.92	28.40	22.57	1.08	0.71	0.65	0.26	0.13	0.25
Avg. weight	47.53	30.56	21.06	1.10	0.32	0.34	0.23	0.21	0.06

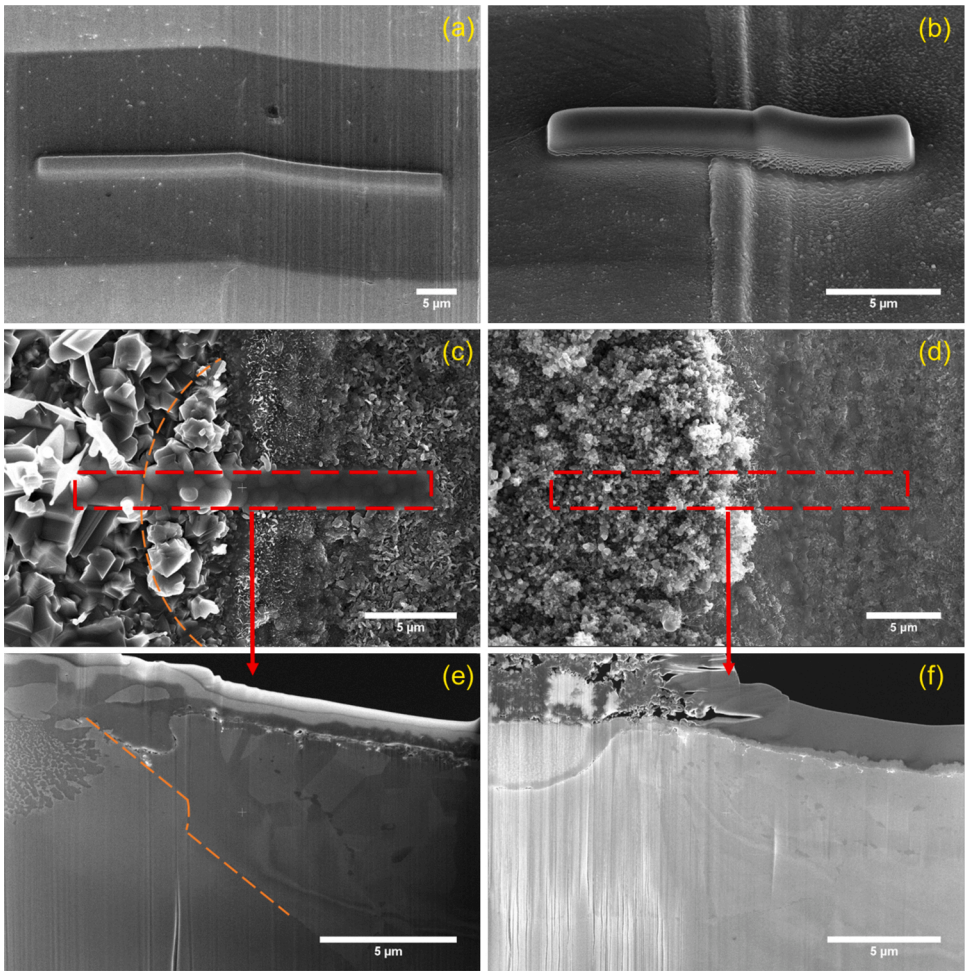

Fig. 1. SEM surface view of polished alloy 800 samples with the right part treated by NS-SPD evolved at four different stages of thermochemical treatment and corrosion testing (a-d), and two TEM lamella prepared by FIB milling from two alloy samples before and after metal dusting corrosion test (e-f). (a) Alloy sample directly after NS-SPD with Pt protection layer deposited in the center. (b) Alloy sample after first preoxidation step (10 % H_2O in Ar, 540 °C, 1 bar, 6 h) with C protection layer deposited in the center. (c) Alloy sample after second preoxidation step (20 % CO, 15 % CO_2, 25 % H_2, 10 % H_2O, 30 % Ar, 750 °C, 20 bar, 20 h) with Pt protection layer deposited within the red square. (d) Alloy sample after 20 h corrosion test (10 % CO in Ar, 550 °C, 1 bar). (e) Cross-section TEM lamella resulting from region below red square in (c). A bulk alloy grain boundary visible on the sample surface is marked with orange dash lines both in (c) and (e). (f) Cross-section TEM lamella prepared from the region below the red square in (d).

this case, the roughening is significantly more pronounced in the polished region. Fig. 1 (e) shows the corresponding TEM lamella. Since a grain boundary was visible in the polished area (marked in Fig. 1 (c)), the lamella preparation could be extended across it while also covering the transition region and the NS-SPD region. The grain boundary can be identified in the SEM cross-section image of the lamella after thinning to electron transparency (marked in Fig. 1 (e)).

An alloy sample subjected to the two-step thermochemical treatment was further tested at metal dusting conditions with infinite carbon activity (a_c >>1) (1 bar 10 % CO in Ar at 550 °C) for 20 h. From the SEM image shown in Fig. 1 (d) it can be seen that the polished area produced a thick layer of metal dusting products including many long carbon filaments and some metal particles. In contrast, the area subjected to NS-SPD before the oxidative thermochemical treatment reveals no visible carbon structures. From comparing the corresponding TEM lamellae shown in Fig. 1 (f) to that of Fig. 1 (e), it can be conjectured that the near surface microstructure in the polished region has transformed, while the NS-SPD region seems to have maintained its overall structural integrity during the corrosion test.

Raman spectroscopy is one of the most sensitive and informative techniques to characterize carbon materials and was applied for non-destructive structural characterization of the deposited carbon [77]. Fig. 2 shows a Raman line scan across an NS-SPD area. The sample is equivalent to that of Fig. 1 (d) and (f), i.e. subjected to metal dusting corrosion testing for 20 h, but also ultrasonically cleaned in acetone for 30 min prior to Raman characterization. Ultrasonication was performed to remove loosely adhered metal dusting products and thereby facilitate the focus of the instrument on the alloy coupon. The Raman spectra show clearly the D-, G- and 2D- bands of carbon formed outside the NS-SPD region [78]. The G and 2D bands originate from crystalline carbon while defect breaks the symmetry in the graphene lattice and gives a D band. In this region, the D band has a higher intensity than the corresponding G band. Previous results have indicated that amorphous carbon is synthesized first on this alloy surface during the corrosion test under CO [79]. There are no peaks originating from carbon structures within the NS-SPD region, and this is the case also before the ultrasonic cleaning in acetone (not shown). At approximately 685 cm^{-1}, there is a band prevailing across the whole Raman line scan, but more intense outside the NS-SPD region than inside. There may also be slight shifts. Bands around this wavelength are often attributed to spinel phases, for

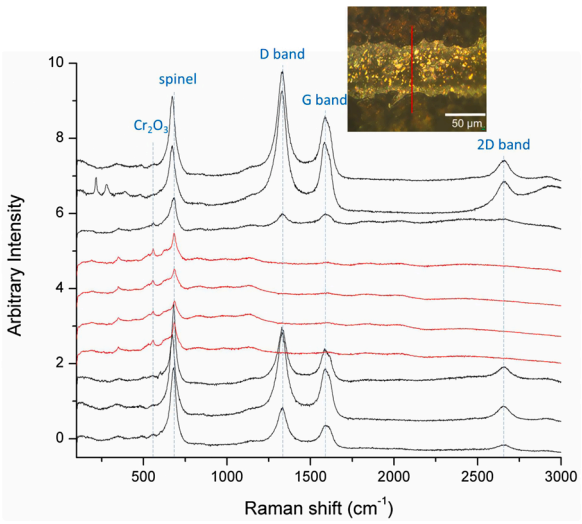

Fig. 2. Raman spectroscopy line scan across the NS-SPD region on an alloy sample subjected to the two-step thermochemical treatment and metal dusting corrosion test for 20 h. The NS-SPD region is the horizontal, bright contrast band in the optical microscopy image. Loosely adhered corrosion products have been removed by ultrasonic cleaning.

which the composition may vary, e.g. Fe_3O_4 or $(Cr, Me)_3O_4$ where Me could be Mn as well as Fe [80,81]. Notably, we can observe a small peak around 558 cm^{-1} within the NS-SPD region, which indicates that this region is rich in Cr_2O_3 [82,83].

To track the development of the alloy through the four stages in further detail, TEM characterization after NS-SPD, thermochemical pretreatments, and metal dusting testing was performed. For reference, we have divided all the TEM lamellae into 3 characteristic regions: the polished surface and the region below (always shown to the left), the NS-SPD region (always shown to the right), and the transition region between these. Elemental mapping by Energy Dispersive X-ray Spectroscopy (EDS)/Electron Energy Loss Spectroscopy (EELS) for each region was obtained to study the composition.

Fig. 3 shows bright field (BF) TEM images from Incoloy 800. The polished, left part of Fig. 1 (a) is shown in cross-section in Fig. 3 (a). Except a sub-surface, straight grain boundary, only a few dislocations can be observed in this region. Fig. 3 (b–d) show cross-section BF TEM images from the NS-SPD region on the right side of Fig. 1 (a). This region is characterized by severe plastic deformation that extends to 8 µm below the surface. In addition to a high density of dislocations, crystal twinning, slip and shear bands are observed (with additional evidence provided in the supplementary information (SI), Figure S1). In Fig. 3 (c) and (d) the material is imaged along the $[1\bar{1}0]$ projection, as demonstrated by the electron diffraction pattern inset in (c). Here it is observed that some of the deformation bands are located on the densely packed (111) planes, which are the slip planes in face centred cubic crystals. Some deformation bands are inclined to the {111} slip planes and are hence pure shear bands. The degree of plastic deformation increases towards the surface, and in the upper half µm (down to the black, dashed line in Fig. 3 (c)) the original single crystal is about to transform into a multi-crystalline, fine-grained surface layer (see also SI, Figure S2). EDS indicates no compositional changes in the NS-SPD region relative to the polished region according to the Fe, Ni, Cr, Al, etc. elemental maps (SI,

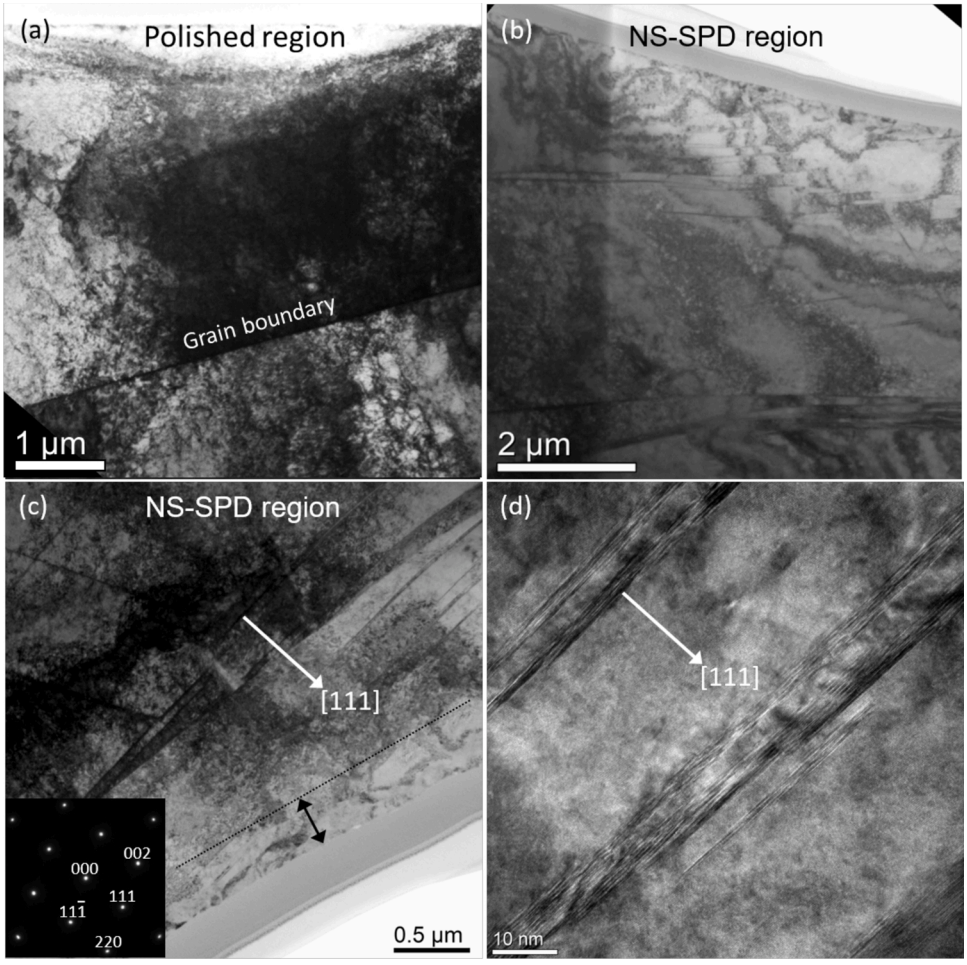

Fig. 3. BF TEM images. (a) Low mangnification image from the polished region. (b-d) all show images from the NS-SPD region. In Figs. (c) and (d) the sample is rotated compared to Figs. (a) and (b). The electron diffraction pattern, inset in (c), is from the $[1\bar{1}0]$ zone axis. The BF TEM images in (c) and (d) are both taken along this projection. The white arrows in (c) and (d) show the (111) plane normal. The deformation bands shown in the high resolution image in (d) are located on the (111) slip planes, common for face centered cubic crystals.

Figure S3).

The near surface region of Incoloy 800 changes upon oxidation in 10 % steam at 540 °C for 6 h. Fig. 4 (a) displays a cross-section BF TEM image of this sample. The three characteristic regions; polished (no NS-SPD), transition and NS-SPD, are included in the cross-section. Elemental distributions are given in Fig. 4 (b–c), where colors have been used to indicate Fe (blue), Ni (green), and Cr or O (red), in order to show the location and overlap of these elements. Comparison of the two RGB (red, green, and blue) color-coded images tells what elements that are oxidized near the alloy surface. Detailed EDS mapping for each region can be found in the supplementary information (SI Figure S4). The images show that the oxide layer is around 20~56 nm in the polished region, and the thickness does not change too much upon moving into the NS-SPD region but varies from 20 to 100 nm due to evolvement of particle-like features (roughness in Fig. 1 (b)). For both the polished and the transition region, iron oxide is covering the surface, with isolated Ni particles in the metallic state distributed on top of this layer. A chromium oxide layer is found under the iron oxide, connected to the alloy matrix with nickel enrichment at the interface. The surface of the NS-SPD region is partially covered by iron oxide particle-like features, and also with a chromium oxide layer below. But here, no metallic nickel particles are found on top of the surface. One should also note that the nickel enrichment at the transition between the oxide layer and alloy matrix is less pronounced. Detailed analysis indicates that the steam oxidation has resulted in a reduced, but not diminished, dislocation density.

Fig. 5 shows changes induced by the second step of the thermo-chemical treatment, i.e. after 20 bar syngas at 750 °C exposure subsequent to the oxidation in steam (540 °C), and is composed of stitched BF STEM images of the lamella from the three defined regions. Corresponding element maps collected from these regions are displayed as RGB element merges in Fig. 5 (b) and (c). It can be observed that the oxide layer evolved in the polished region to the left is composed of two distinct zones; an inner oxide that appears to have grown into the alloy matrix up to ca. 4.2 μm and an outer layer that extends above the original polished surface to ca. 2.8 μm. By comparison of the two RGB element merges in Fig. 5 (b) and (c), it can be observed that a thick Fe oxide is covering the polished region, and this external oxide becomes thinner when extending to the transition region. Large, metallic Ni particles (1−2 μm) are wrapped by the external oxide. The internal oxides formed intra-granularly on either side of the grain boundary (indicated by the dashed line in Fig. 1 (e)) exhibit very different morphologies. The internal oxide on the left side of the grain boundary that extends relatively deep into the alloy is rich in Cr and contains some Fe (SI, Figure S5). It is clearly dispersed by a metallic, Ni interconnected network. This may be compared to the isolated Ni islands within the

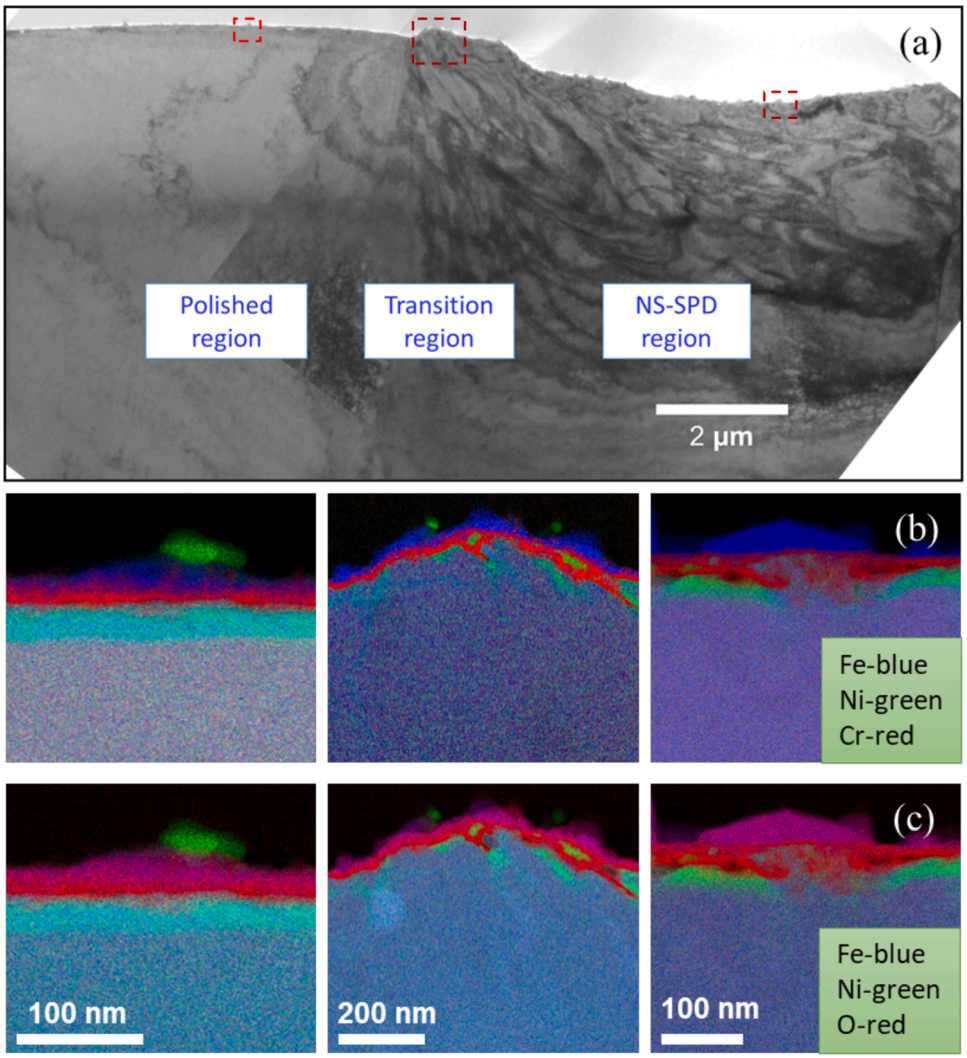

Fig. 4. Lamella prepared by FIB milling from sample with right part treated by NS-SPD after first preoxidation step (10 % H_2O in Ar, 540 °C, 1 bar, 6 h), as indicated in Fig. 1 (b): (a) Stitched bright field transmission electron microscopy (TEM) images with selected areas corresponding to the polished, transition and NS-SPD regions marked by red dash squares for EDS analysis. (b-c) RGB color-coded EDS images of the three regions.

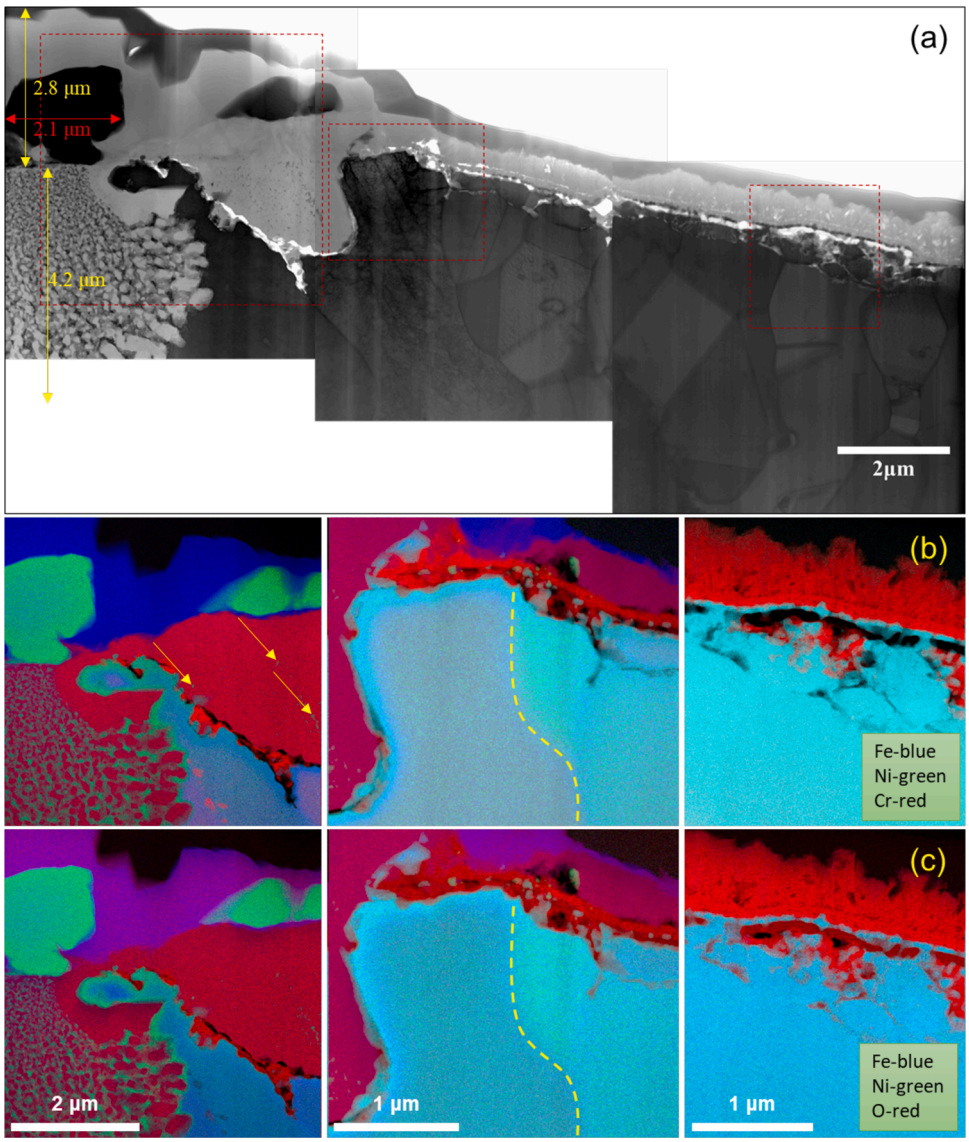

Fig. 5. Lamella from sample with right part treated by NS-SPD after second preoxidation step (20 % CO, 15 % CO_2, 25 % H_2, 10 % H_2O, 30 %Ar, 750 °C, 20 bar, 20 h), as indicated in Fig. 1 (c) and (e). (a) Stitched, BF STEM image with selected areas corresponding to the polished, transition and NS-SPD regions marked by red dashed squares for EDS analysis. (b-c) RGB color-coded EDS images of the three regions.

predominantly Cr containing oxide on the right side of the grain boundary (indicated by an arrow in Fig. 5 (b), see also SI Figure S5). This oxide is close to the transition region and surrounded by numerous deformation twins on its right side.

The details of the transition region between the polished surface and the NS-SPD region can be observed in the middle of Fig. 5 (a). We assume that the border of the NS-SPD impact is found in the middle of the red-dashed square since the surface is depressed at the right side from this point and the region below is associated with a finer grain structure (grain size 1−2 µm). The abovementioned deformation twins are found just on the left side of this border, indicating that the effect of NS-SPD is not confined to the region just below the impact. Nevertheless, the Cr and Mn contents are depleted to the right of the border (yellow dash line, Fig. 5 (b) and (c)) as compared to the left side. It should be noted that the external oxide layer on the top of the sample becomes thinner (200−500 nm) in the NS-SPD region than in the polished region (ca.3 µm). Compared with the external oxide above the polished region that contains mainly Fe_3O_4 (as identified with combined TEM and magnetic test), the layer on top of the transition region shows a thinner Fe_3O_4 oxide together with a relatively thick Cr-rich oxide. Detailed EDS reveals that the latter also contains Mn and that internal oxidation is limited to Si and Al at the interface between the oxide layer and the bulk alloy (see SI, Figure S5). Voids are also present at the interface.

The cross-section view confirms that the surface of the NS-SPD region on the right has also become rougher compared with the sample after the second step of the heat treatment, as previously inferred by SEM. The two sets of RGB color-coded images in Fig. 5 (b) and (c) show that – in contrast to the polished region - the NS-SPD region is covered by an oxide layer containing predominantly Cr and depleted of Fe and Ni. A thin (ca. 80 nm) Fe and Ni rich layer can be observed under the dense, Cr-rich layer. By comparing the EDS maps, one may conjecture that Fe and Ni are not oxidized in this region (see also SI, Figure S5). It may be assumed that this Fe-Ni layer represents the surface after the NS-SPD, now existing between the external and the internal oxides and more corrugated than what could be observed in Figs. 3 and 4. Close examination indicates that the first 80–100 nm of Cr oxide just above the Fe and Ni is relatively dense, while a thicker (upper 210 ~ 560 nm), rougher and less dense oxide resides on top of the compact layer. Si, Al, Cr, Mn, and O can be observed under the Fe-Ni layer in the EDS mapping (see Figure S4), representing various internal oxides. Fine grains (grain

size 1−2 μm) of irregular shapes can be observed under the NS-SPD surface and this grain structure starts exactly on the right side of the yellow dash line marked in Fig. 5 (b) and (c), assumed above as the boundary of the NS-SPD impact. Figure S6 shows an ultrasonically cleaned sample with the middle area treated by NS-SPD after the two-step thermochemical treatment and subsequent 20 h metal dusting corrosion test (10 % CO in Ar, 550 °C, 1 bar). The original grain size of the alloy is between 30−70 μm, while grain refinement occurred in the middle area and the grain size reduced to 1−3 μm. One should also note that two small voids are present at the interface of the oxide and the bulk which probably were created when applying the NS-SPD treatment.

Detailed STEM/EDS analyses of the lamella from the coupon showed in Fig. 1 (d), subjected to severe metal dusting conditions with infinite carbon activity ($a_c >> 1$) for 20 h after the two-step thermochemical treatment, are displayed in Fig. 6. An amorphous carbon layer was applied to the area of interest on top of the sample to preserve the surface morphologies – including the carbon filaments formed - during preparation by FIB. The elemental maps are provided as RGB element merges in Fig. 6 (b) and (c) and as separate EDS elemental maps in the supporting information (SI, Figure S7).

Fig. 6 displays Cr-containing internal oxides in the polished region that bear a strong resemblance to those found after the two-step thermochemical treatment (i.e. before CO exposure). However, a continuous band at the interface between the internal oxide and the metal alloy matrix has no Ni rich network. There is no indication of an external oxide at the surface, only smaller, dispersed iron particles and larger Ni particles, as well as some regions containing both elements. Corrosion products containing C, Fe and Ni particles can be observed on top of the polished surface (SI, Figure S7(a)). The transition region contains Fe at the surface, of which some are associated with a Cr-containing surface oxide and some with the corrosion products on top. The Cr oxide gets slightly thinner upon moving into the NS-SPD region (see also SI, Figure S7 (b)). The border between the NS-SPD region and the polished region of this sample is not that clear, but we register a difference in the EDS map contrast between the left and right sides, with slightly less Cr and Mn in the near surface of the NS-SPD region (SI, Figure S7(b)). Even though the surface has been covered by a carbon coating before FIB and thereafter subjected to thinning, carbon filaments are visible on the surface of the polished and transition regions (Fig. 6). For the C signal, we see that wherever Fe is present on the surface, there are also carbon filaments. By comparing the EDS signal of O, Cr, Mn, Fe and Ni we observe that Cr and Mn are overlapped to a large extent. This is even the case with respect to precipitates in the bulk of the alloy, which are correspondingly depleted in Ni and Fe.

The NS-SPD region basically shows little or no dissimilarity compared to the sample representing the state before the corrosion test, i.e. a thin (100−600 nm) Cr-rich oxide still covers the surface. Neither carbon filaments nor carbon-containing phases could be found in the NS-

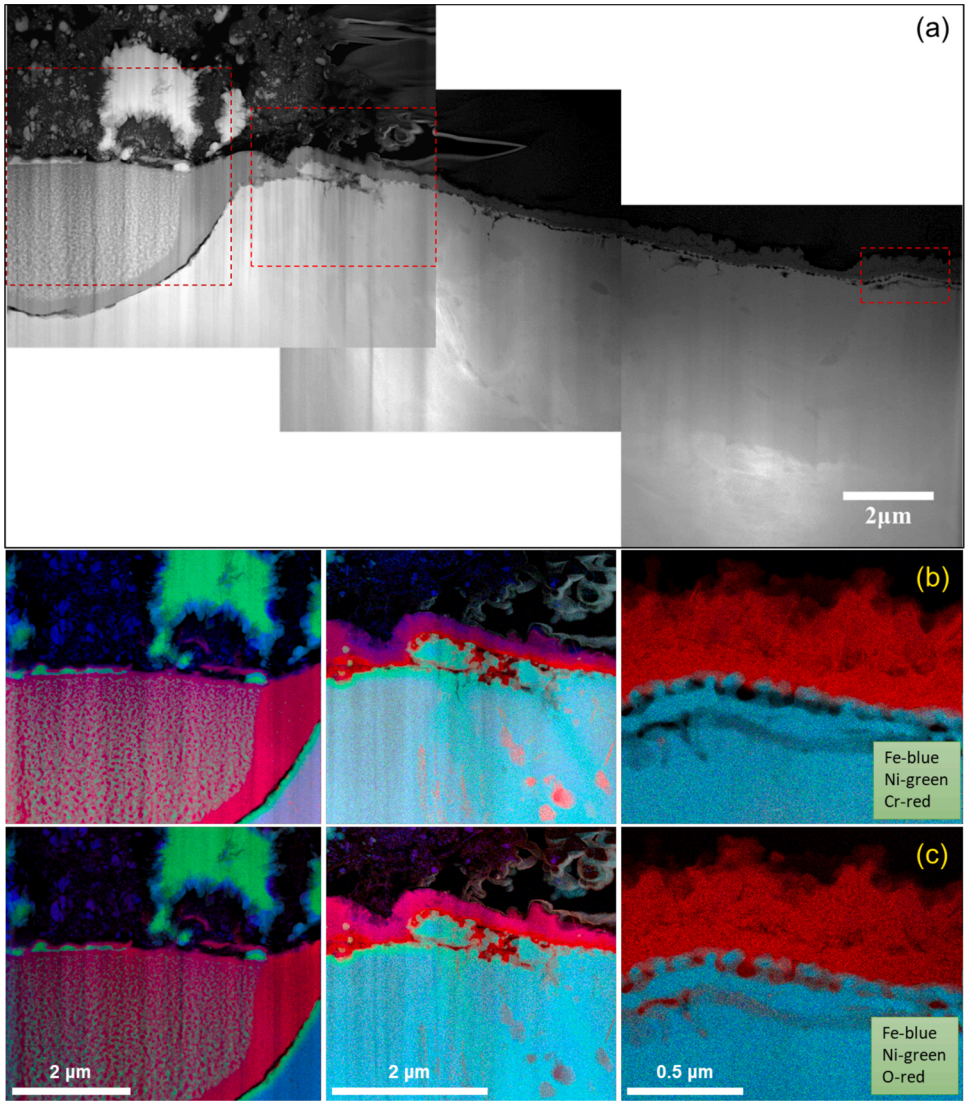

Fig. 6. Lamella from sample with right part treated by NS-SPD after the two-step thermochemical treatment and subsequent 20 h metal dusting corrosion test (10 % CO in Ar, 550 °C, 1 bar), as indicated in Fig. 1 (d) and (f): (a) Stitched, high angle annular dark field scanning transmission electron microscopy (HAADF STEM) image with selected areas corresponding to the polished, transition and NS-SPD regions marked by red dashed squares for EDS analysis. (b-c) RGB color-coded EDS images of the three regions.

SPD region, likewise, no Fe or Ni particles. The alloy matrix below the oxide displays a fine-grained structure, extending about 8 μm into the bulk. It may even be inferred that the surface oxide thickness correlates with the grain structure. A relatively thin Cr-rich oxide can be seen away from any grain boundaries in the STEM image in Fig. 6, while a thicker oxide is observed directly above the grain boundaries (grain size better visualized in SI, Figure S8). From the top view of the NS-SPD region both in Fig. 1 (c) and (d) we can see that the surface is corrugated in a way that seems to reflect the underlying grain structure, with accumulation of oxide flakes along the grain boundaries (see also NS-SPD region in the focused image in Figure S9). The EDS mapping generally reveals that Al and Si oxides are present at the interface between the Cr-rich oxide phases and the alloy matrix in all regions.

The metal dusting corrosion test with infinite carbon activity (a_c >>1) was extended to 100 h for one additional sample, and a TEM lamella prepared. Fig. 7 shows the changes induced by prolonged exposure to the carburizing atmosphere. From SEM images (SI, Figure S10) of the sample, we can see that the polished region produced more corrosion products than the 20 h exposure, essentially a carbonaceous layer of around 20 μm thickness. It can further be concluded that the NS-SPD region has no observable carbon filaments on the surface. Raman spectra also confirmed that absence of carbon in the NS-SPD region (see SI, Figure S11). Fig. 7 (a) shows the SEM images, and the corresponding EDS RGB element merges, with the detailed and extended EDS mapping displayed in the Supplementary Information (SI, Figure S12). In the polished region, it can be observed that all the external oxide and significant parts of the internal oxides have disappeared to form a pit. Furthermore, carbon filaments are found directly attached to the remaining internal oxide. A thin iron oxide layer is present in the transition region with some carbon filaments on top. With respect to the NS-SPD region, it appears that the thin, Cr-rich, oxide layer has maintained during the prolonged test. Close examination, however, reveals a few, very small metallic Ni particles that can be observed as green dots on top of the Cr-rich oxide in Fig. 7 (b–c).

The loosely adhered metal dusting corrosion products were ultrasonically removed from the alloy and subjected to TEM analysis for both 20 and 100 h carburizing exposures, and results for the former are displayed in Figure S13. The carbon presents a variety of filamentous structures, i.e. graphitic sheets arranged to different degrees of order. Beyond carbon, Fe, Ni, Cr, and O are present in the corrosion product. Cr oxide is mixed with the carbon material. Close inspection reveals that the main element found inside the filamentous carbon structures is Fe. Spectroscopy mapping further confirms that the main part of the Fe is not present as oxide. However, in a number of filamentous structures Fe oxide seems to exist at one end, indicating incomplete reduction. The amount of Ni in the corrosion product is significantly less than Fe, and appears as mixed with the carbon and the Cr oxide, i.e. we cannot uniquely associate it with the core of the carbon filaments.

4. Discussion

Neither carbon filaments nor carbide is found in the near surface

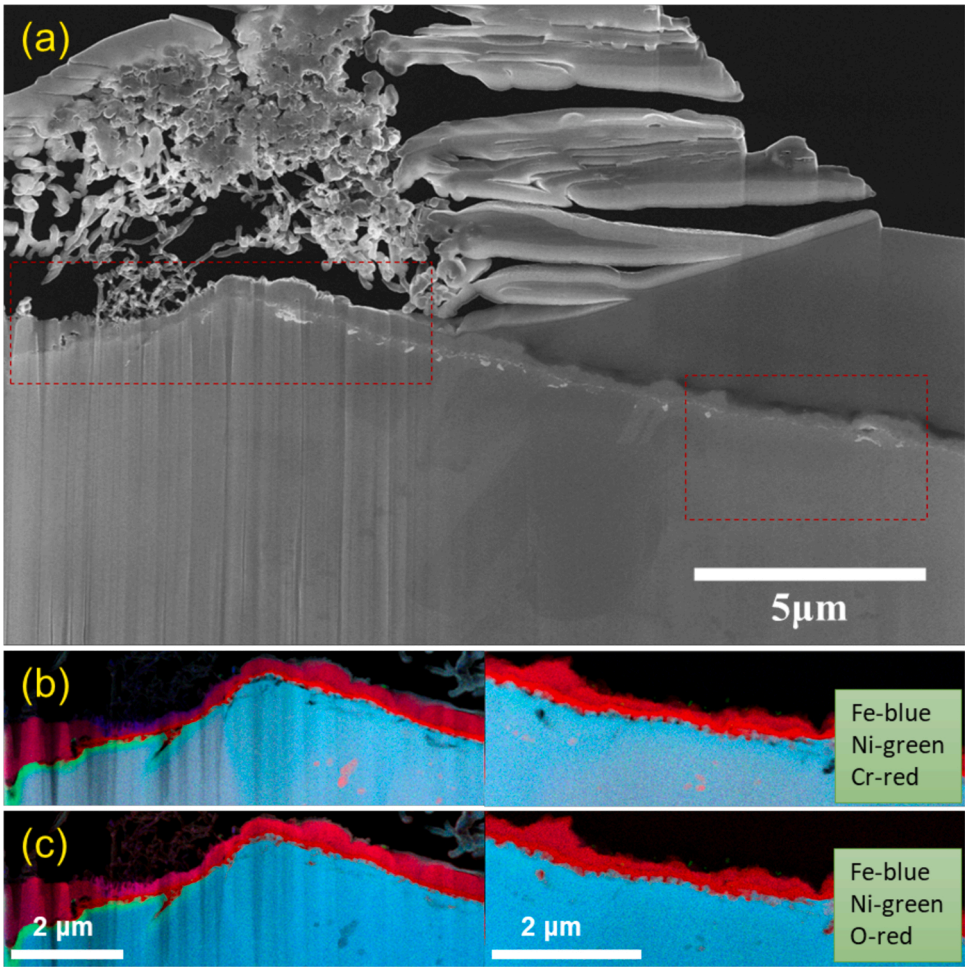

Fig. 7. Lamella from sample with right part treated by NS-SPD after the two-step thermochemical treatment and subsequent 100 h metal dusting corrosion test (10 % CO in Ar, 550 °C, 1 bar): (a) Scanning electron microscope (SEM) images with selected areas corresponding to the polished, transition and NS-SPD regions marked by red dash squares for EDS analysis. (b-c) RGB color-coded EDS images of the three regions.

severe plastic deformation (NS-SPD) region after testing under a gas mixture with infinite carbon activity (10 % CO in Ar). This indicates that the fine-grained, relatively thin Cr oxide scale produced by the combined NS-SPD and thermochemical treatment on Incoloy 800 considerably improved the metal dusting corrosion resistance relative to the polished (non NS-SPD) region subjected to the same thermochemical treatment. NS-SPD treatment alone is not sufficient to obtain the same protection and the same holds if combined only with the first oxidation step, i.e. in 10 % steam in Ar at 540 °C. In fact, both steps are critical in order to form a scale of favourable structure, composition and thickness following the NS-SPD impact. It is difficult to provide a complete and fully consistent explanation for this, but the stepwise developments in microstructure and local composition can provide some understanding.

A dense and well-adherent Cr-rich oxide scale seems to provide optimum protection against carburization [19,34,36,74]. This scale should be thick enough to shield the underlying matrix. But it should not be too thick since that usually enhances incompatibility in thermal expansion between the oxide and the underlying bulk alloy that may over time cause cracks or detachment. From the results described here as well as others [23,32,84], it may be concluded that Fe and Ni phases should not be present in the oxide scale since, upon reduction, these elements can catalyze carbon deposition from the process gas. Common oxidation processes often yield oxide scales comprising an outer layer rich in Fe [30,85]; such as that we observed in the polished region. This can be related to a strongly oxidizing environment combined with insufficient transfer of Cr towards the surface. It should be noted that the mixture applied in the second step of the thermochemical treatment essentially constitutes a model synthesis gas, hence not so different from the composition prevailing under typical industrial conditions for which we have previously observed carbon formation of non NS-SPD samples of Incoloy 601 at temperatures of 650 °C and 750 °C [86]. The $a_c >> 1$ condition was therefore applied to provoke carbon formation. We infer that the mixture of reducing and oxidizing gases in conjunction with the temperature facilitates the selective formation of Cr oxide at the surface given that the transport of Cr is efficient in the near surface region of the alloy. Moreover, the thermochemical treatment is not too harsh, thereby enabling the formation of a dense and seemingly well-adhered layer. The NS-SPD treatment evidently enables Cr diffusion to a larger extent than a grain structure not impacted by this treatment.

Our mechanical treatment of the alloy surface introduces subsurface deformation, which creates dislocations and other defects in the crystal lattice. It is well established that the presence of dislocations influences the properties of an alloy [74,85]. Here, the subsurface dislocations promoted by plastic deformation are persistent during the first (low--temperature) thermochemical treatment. An ultrafine grain structure is then developed through a recrystallization process in the following thermochemical treatment at higher temperature. The grain boundary density is thereby significantly increased in the region impacted by NS-SPD. Grain boundaries (and defects) have distinct properties relative to the bulk lattice in terms of atomic coordination and diffusion rates [55]. In Cr-containing alloys, dislocations and grain boundaries have been found to provide rapid diffusion pathways for chromium atoms, allowing this metal to reach the surface and form a protective oxide scale [71,74]. In this work, Cr oxide at the surface of the alloy becomes gradually more prominent within the transition region upon approaching the NS-SPD region, which indicates that the NS-SPD impact has local effects and becomes weaker when far from the processed region. The transition region also shows a content difference of Ni and Fe that probably results from the depletion of Cr and Mn under the NS-SPD impacted surface (Figs. 5 and S3 (b)). The Cr oxide thickness in the NS-SPD region even correlates locally with the density of grain boundaries and the distance from a grain boundary, which further underlines that the intragranular and surface Cr diffusion rates are low. This is in agreement with other work showing that the oxide composition and thickness both depend on the underlying micro-structure [87,88].

External oxidation in the NS-SPD region yields almost exclusively a Cr rich oxide with some Mn, while internal oxidation is limited to Si and Al along a narrow zone below the Cr rich oxide layer. SiO_2 and Al_2O_3 are both dense oxides with the ability to hinder further inward oxidation, while at the same time stopping Fe and Ni from diffusing into the scale [35]. The presence of Mn in the Cr oxide may be explained by relatively high mobility of Mn in Cr_2O_3 and concurring formation of spinel [22]. The scale may hence be a (non-stoichiometric) mixed oxide, or composed of different Cr rich phases, e.g. Cr_2O_3 and $MnCr_2O_4$ [22,88].

In the polished region, external oxidation yields Fe_3O_4 that covers most of the non-NS-SPD treated surface of the sample. Internal oxidization clearly resulted in two kinds of Cr oxides beside the grain boundary indicated in Fig. 1 (e). The left oxide is highly interdispersed with metallic Ni, possibly also some Fe, and penetrates deep into the bulk, while the oxide to the right is shallow and almost without interdispersion. It is likely that the oxide growth is affected by the local internal structure; i.e. grain boundaries and defects, since the internal oxidation is associated with volume increase that produces compressive stress [85]. High compressive stresses may eventually result in intergranular embrittlement and fracture [85]. Here, grain boundary migration possibly occurs due to the internal oxide and the compressive stresses generated on the right side [85]. Moreover, stress relief can be achieved by the outward transport of Ni and Fe [85,89]. Ni is clearly enriched adjacent to the internal oxides and exhibits a seemingly interconnected network. Ni-rich phases at the oxide-metal interface are claimed to aid in transporting Ni and Fe to the surface [85,90]. External growth of the Fe_3O_4 scale by outward Fe diffusion may also result in vacancies being injected into the alloy at the scale-alloy interface. Combined, this facilitates outward diffusion of metal (Fe, Ni) atoms and accommodation of the volume increase during internal oxidation [91].

According to the EDS mapping. (SI, Figure S3), there is no change in alloy composition due to the NS-SPD treatment at room temperature. After the first step of the thermochemical treatment, Ni particles could be observed in the polished region and transition region but not in the NS-SPD region. Some Fe oxide is found in all regions, however. After the second step, there are significant differences between the NS-SPD region and the polished region (Fig. 1 (c), (e) and Fig. 5). Two types of Ni-rich particles can be observed above the polished surface (Fig. 5). By comparing the two types, we observe that the one to the left seems to have grown from the original polished surface and is still connected to the network inside the internal oxide. For those to the right, it may be inferred that increased volume from Cr oxide formation and external Fe oxidation lifted them above the original polished surface. In addition, the Ni-rich particles above the original polished surface were found to have a higher amount of Fe in the centre of the particles and a higher amount of Ni at the surface (Figure S5 (a)). This may indicate a gradual de-alloying of the particles that also releases Fe to the external oxide. In the NS-SPD region, the efficient supply of Cr combined with the gas mixture composition of the second step lead to the reduction of the Fe oxide on the surface.

After heat treatment, SiO_2 and Al_2O_3 are present as a thin layer at the scale-substrate interface, in accordance with other observations [5]. It has been reported that alloys that contain Al and Si show the best metal dusting corrosion resistance among 13 alloys studied, indicating that Al_2O_3 and SiO_2 scales play an important role in preventing metal dusting attack [23]. Si and Al can be oxidized selectively in the very first hours of heat treatment, forming nuclei and islands of oxide which could inhibit carbon ingress [5].

After the metal dusting corrosion test, cross section SEM images (Fig. 1 (d) and (f)) showed that the external crystal-like features were decomposed and carbon filaments are visible over the polished region and the transition region, while the NS-SPD region maintained a thin oxide layer without carbon deposition. For the C signal, we see that where there is Fe, there are more carbon filaments formed. In the polished region, the external Fe_3O_4 oxide was hence reduced to metal particles acting as catalysts for carbon formation [14,92,93] upon exposure to 10 % CO in Ar. The Ni rich particles that were covered by

Fe_3O_4 also started to fragment. Cr oxide is also found in the corrosion product (SI, Figure S13). This is likely because the Ni and Fe network within the internal Cr oxide can transport C into the bulk of the alloy, and some Cr oxide particles become detached from the matrix through the resulting carburization and disintegration.

Summarized, combined NS-SPD and thermochemical treatment yield a metal dusting corrosion-resistant surface under infinite carbon activity. Our results imply that a thin and dense Cr-rich oxide layer could be sufficient, but the optimum thickness, grain structure, and composition of such a scale remain to be established. Its formation requires high dislocation and grain boundary densities in conjunction with thermochemical treatment that allows efficient Cr transfer. Oxide formation beyond the preferred Cr rich phases is further suppressed by limiting the oxygen chemical potential. We believe that the phenomena observed can be developed commercially as a new pretreatment method for materials or process equipment, or even as a materials recovery routine during plant interruptions. The findings may have impact beyond metal dusting corrosion, for example in steam generators [47,58,85], ethylene crackers [94] and supercritical water-cooled reactors [42] where a dense Cr-rich oxide scale is also highly demanded. Since internal oxidation is prevented in the NS-SPD region, this method may also inhibit internal inter-granular oxidation embrittlement [85].

5. Conclusion and outlook

The metal dusting corrosion resistance of Fe- based alloy (Incoloy 800) has been successfully improved by combined NS-SPD and thermochemical treatment. NS-SPD impact introduces a higher density of dislocations and other defects in the crystal lattice. An ultrafine grain structure is then developed through a recrystallization process in the following thermochemical treatment at higher temperature. Dislocations and grain boundaries provide rapid diffusion paths for Cr that promote the formation of a protective Cr rich oxide layer which prevents carbon formation during exposure to the gas mixture with infinite carbon activity. Meanwhile, the polished (non-NS-SPD) region in the same alloy samples developed both external (mainly Fe_3O_4) and deep internal (Cr rich) oxides during the thermochemical treatment. Such oxides are partly reducible and not able to suppress carbon formation and subsequent ingress, and significant amounts corrosion products were found after exposure to the strongly carburizing atmosphere. In conclusion, combined NS-SPD and thermochemical treatment is a very promising method for metal dusting inhibition that could possibly be extended to other types of corrosions where a protective scale is desired.

Data availability

The raw/processed data required to reproduce these findings cannot be shared at this time due to technical or time limitations.

CRediT authorship contribution statement

Xiaoyang Guo: Conceptualization, Methodology, Validation, Formal analysis, Investigation, Data curation, Writing - original draft, Writing - review & editing, Visualization. **Per Erik Vullum:** Methodology, Validation, Formal analysis, Investigation, Resources, Data curation, Writing - review & editing, Visualization. **Hilde J. Venvik:** Conceptualization, Methodology, Resources, Writing - review & editing, Supervision, Project administration, Funding acquisition.

Declaration of interests

The authors declare that they have no known competing financial interests or personal relationships that could have appeared to influence the work reported in this paper. Please, however, be informed that part of the findings in this paper also have formed the basis for a patent (European Patent Office PCT Patent Application No. PCT/EP2020/075555) from the Norwegian University of Science and Technology (NTNU).

Acknowledgements

The financial support of Research Council of Norway (RCN) under the GASSMAKS research program (Contract No. 233869/E30) is gratefully acknowledged. This publication also forms a part of the iCSI (industrial Catalysis Science and Innovation) Centre for Research-based Innovation, which receives financial support from RCN under Contract No. 237922. The TEM work was carried out on NORTEM infrastructure, RCN Contract No. 197405, TEM Gemini Centre, Norwegian University of Science and Technology (NTNU), Norway. The Research Council of Norway is acknowledged for the support to the Norwegian Micro- and Nano-Fabrication Facility, NorFab, RCN Contract No. 245963/F50.

Appendix A. Supplementary data

Supplementary material related to this article can be found, in the online version, at doi:https://doi.org/10.1016/j.corsci.2021.109702.

References

[1] M.P. Ryan, D.E. Williams, R.J. Chater, B.M. Hutton, D.S. McPhail, Why stainless steel corrodes, Nature 415 (6873) (2002) 770–774.
[2] P. Marcus, Corrosion Mechanisms in Theory and Practice, Crc Press, 2011.
[3] H. Grabke, R. Krajak, E. Müller-Lorenz, Metal dusting of high temperature alloys, Mater. Corros. 44 (3) (1993) 89–97.
[4] H. Grabke, R. Krajak, J.N. Paz, On the mechanism of catastrophic carburization: 'metal dusting', Corros. Sci. 35 (5-8) (1993) 1141–1150.
[5] H.J. Grabke, Metal dusting, Mater. Corros. 54 (10) (2003) 736–746, https://doi.org/10.1002/maco.200303729.
[6] B. Schmid, N. Aas, Ø. Grong, R. Ødegård, In situ environmental scanning electron microscope observations of catalytic processes encountered in metal dusting corrosion on iron and nickel, Appl. Catal. A: Gen. 215 (1) (2001) 257–270.
[7] C. Chun, J. Mumford, T. Ramanarayanan, Mechanisms of metal dusting corrosion of iron, J. Electrochem. Soc. 149 (7) (2002) B348–B355.
[8] P. Szakálos, Mechanisms of Metal Dusting, KTH, 2004.
[9] Z. Zeng, K. Natesan, V.A. Maroni, Investigation of metal-dusting mechanism in Fe-base alloys using raman spectroscopy, x-ray diffraction, and electron microscopy, Oxid. Met. 58 (1/2) (2002) 24.
[10] T.S. Hummelshøj, Mechanisms of Metal Dusting Corrosion, Technical University of Denmark (DTU), 2010.
[11] D. Young, J. Zhang, Understanding metal dusting mechanisms, ECS Trans. 16 (44) (2009) 3–15.
[12] A. Fabas, D. Monceau, C. Josse, P. Lamesle, A. Rouaix-Vande Put, Mechanism of metal dusting corrosion by pitting of a chromia-forming alloy at atmospheric pressure and low gas velocity, Corros. Sci. 107 (2016) 204–210, https://doi.org/10.1016/j.corsci.2016.02.033.
[13] M. Szkodo, G. Gajowiec, Studies of the mechanism of metal dusting of 10CrMo9-10 steel after 10 years of operation in the semi-regenerative catalytic reformer, Corros. Sci. 102 (2016) 279–290, https://doi.org/10.1016/j.corsci.2015.10.016.
[14] D.J. Young, J. Zhang, C. Geers, M. Schütze, Recent advances in understanding metal dusting: a review, Mater. Corros. 62 (1) (2011) 7–28, https://doi.org/10.1002/maco.201005675.
[15] H. Grabke, Thermodynamics, mechanisms and kinetics of metal dusting, Mater. Corros. 49 (5) (1998) 303–308.
[16] H. Yin, J. Zhang, D.J. Young, Effect of gas composition on coking and metal dusting of 2.25Cr–1Mo steel compared with iron, Corros. Sci. 51 (12) (2009) 2983–2993, https://doi.org/10.1016/j.corsci.2009.08.026.
[17] M. Stroosnijder, R. Mevrel, M. Bennett, The interaction of surface engineering and high temperature corrosion protection, Mater. High Temp. 12 (1) (1994) 53–66.
[18] H. Grabke, E. Müller-Lorenz, Protection of high alloy steels against metal dusting by oxide scales, Mater. Corros. 49 (5) (1998) 317–320.
[19] K. Voisey, Z. Liu, F. Stott, Inhibition of metal dusting of Alloy 800H by laser surface melting, Appl. Surf. Sci. 252 (10) (2006) 3658–3666.
[20] S.J.M.P. Kurihara, Resistance of Ni-base alloy UNS N 06696 to metal dusting, Mater. Perform. 50 (8) (2011) 66–70.
[21] S. Madloch, A. Dorcheh, M. Galetz, Effect of pressure on metal dusting initiation on alloy 800H and alloy 600 in CO-rich syngas, Oxid. Met. 89 (3–4) (2018) 483–498.
[22] R. Lobnig, H. Schmidt, K. Hennesen, H. Grabke, Diffusion of cations in chromia layers grown on iron-base alloys, Oxid. Met. 37 (1-2) (1992) 81–93.
[23] Z. Zeng, K. Natesan, M. Grimsditch, Effect of oxide scale compositions on metal dusting corrosion of Fe-based alloys, Corrosion 60 (7) (2004) 632–642.
[24] S. Strauss, H. Grabke, Role of alloying elements in steels on metal dusting, Mater. Corros. 49 (5) (1998) 321–327.
[25] C. Rosado, M. Schütze, Protective behaviour of newly developed coatings against metal dusting, Mater. Corros. 54 (11) (2003) 831–853, https://doi.org/10.1002/maco.200303736.

[26] I. Wolf, H. Grabke, A study on the solubility and distribution of carbon in oxides, Solid State Commun. 54 (1) (1985) 5–10.
[27] H. Grabke, E. Muller-Lorenz, S. Strauss, E. Pippel, J. Woltersdorf, Effects of grain size, cold working, and surface finish on the metal-dusting resistance of steels, Oxid. Met. 50 (3) (1998) 241–254.
[28] C. Toh, P. Munroe, D. Young, Metal dusting of Fe–Cr and Fe–Ni–Cr alloys under cyclic conditions, Oxid. Met. 58 (1-2) (2002) 1–21.
[29] L.W. Finger, R.M. Hazen, Crystal structure and isothermal compression of Fe2O3, Cr2O3, and V2O3 to 50 kbars, J. Appl. Phys. 51 (10) (1980) 5362–5367.
[30] M.W. Edwards, N.S. McIntyre, Gas phase initial oxidation of incoloy 800 surfaces, Oxid. Met. 79 (1–2) (2013) 179–200.
[31] E. Essuman, G. Meier, J. Żurek, M. Hänsel, W. Quadakkers, The effect of water vapor on selective oxidation of Fe–Cr alloys, Oxid. Met. 69 (3-4) (2008) 143–162.
[32] Z. Zeng, K. Natesan, Initiation of metal-dusting pits and a method to mitigate metal-dusting corrosion, Oxid. Met. 66 (1–2) (2006) 1–20, https://doi.org/10.1007/s11085-006-9032-z.
[33] P. Wilson, Z.J.Cs. Chen, The effect of manganese and chromium on surface oxidation products formed during batch annealing of low carbon steel strip, Corros. Sci. 49 (3) (2007) 1305–1320.
[34] H. Li, W. Chen, High temperature carburization behaviour of Mn–Cr–O spinel oxides with varied concentrations of manganese, Corros. Sci. 53 (6) (2011) 2097–2105.
[35] H. Li, W. Chen, Stability of MnCr2O4 spinel and Cr2O3 in high temperature carbonaceous environments with varied oxygen partial pressures, Corros. Sci. 52 (7) (2010) 2481–2488.
[36] H. Li, Y. Zheng, L.W. Benum, M. Oballa, W. Chen, Carburization behaviour of Mn–Cr–O spinel in high temperature hydrocarbon cracking environment, Corros. Sci. 51 (10) (2009) 2336–2341.
[37] T. A. Ramanarayanan and C. Chun, "Metal dusting resistant alloys," ed: Google Patents, 2004.
[38] B. Bao, J. Liu, H. Xu, B. Liu, W. Zhang, Inhibitory effect of MnCr 2 O 4 spinel coating on coke formation during light naphtha thermal cracking, RSC Adv. 6 (73) (2016) 68934–68941.
[39] S. Kumar, G. Mahobia, The features of metal dusting process in the extremely low nickel austenitic stainless steel (18Cr-21Mn-0.65 N-Fe), Corros. Sci. 176 (2020) 108926.
[40] M. Li, Y. Zhu, C. Zhou, Effect of yttrium on the coking behavior of Fe-based superalloy in heavy hydrocarbon, Corros. Sci. 98 (2015) 81–87.
[41] J.C. Walmsley, J.Z. Albertsen, J. Friis, R.H. Mathiesen, The evolution and oxidation of carbides in an Alloy 601 exposed to long term high temperature corrosion conditions, Corros. Sci. 52 (12) (2010) 4001–4010, https://doi.org/10.1016/j.corsci.2010.08.015.
[42] M. Fulger, D. Ohai, M. Mihalache, M. Pantiru, V. Malinovschi, Oxidation behavior of Incoloy 800 under simulated supercritical water conditions, J. Nucl. Mater. 385 (2) (2009) 288–293.
[43] M. Yamawaki, M. Mito, M. Kanno, Oxidation of heat-resistant Fe-base incoloy 800 alloy, Trans. Jpn. Inst. Met. 18 (8) (1977) 567–573.
[44] Z. Zeng, K. Natesan, Z. Cai, D. Gosztola, R. Cook, J. Hiller, Effect of element diffusion through metallic networks during oxidation of Type 321 stainless steel, J. Mater. Eng. Perform. 23 (4) (2014) 1247–1262.
[45] X. Li, K. Lu, Playing with defects in metals, Nat. Mater. 16 (2017) 700–701.
[46] K. Ralston, N. Birbilis, C. Davies, Revealing the relationship between grain size and corrosion rate of metals, Scripta Mater. 63 (12) (2010) 1201–1204.
[47] A. Paul, K. Kaimal, M. Naik, S. Dharwadkar, Lattice and grain boundary diffusion of chromium in superalloy Incoloy-800, J. Nucl. Mater. 217 (1–2) (1994) 75–81.
[48] Y. Estrin, A. Vinogradov, Extreme grain refinement by severe plastic deformation: a wealth of challenging science, Acta Mater. 61 (3) (2013) 782–817.
[49] A. Vinogradov, Y. Estrin, Analytical and numerical approaches to modelling severe plastic deformation, Prog. Mater. Sci. 95 (2018) 172–242.
[50] N. Tsuji, Y. Saito, S.H. Lee, Y. Minamino, ARB (Accumulative Roll-Bonding) and other new techniques to produce bulk ultrafine grained materials, Adv. Eng. Mater. 5 (5) (2003) 338–344.
[51] L. Ke, L. Jian, Surface nanocrystallization (SNC) of metallic materials-presentation of the concept behind a new approach, J. Mater. Sci. Technol. 15 (3) (1999) 193–197.
[52] R. Gupta, N. Birbilis, The influence of nanocrystalline structure and processing route on corrosion of stainless steel: a review, Corros. Sci. 92 (2015) 1–15.
[53] H. Gleiter, Nanostructured materials: basic concepts and microstructure, Acta Mater. 48 (1) (2000) 1–29.
[54] G. Palumbo, S. Thorpe, K. Aust, On the contribution of triple junctions to the structure and properties of nanocrystalline materials, Scr. Metall. Mater. 24 (7) (1990) 1347–1350.
[55] K. Ralston, N. Birbilis, Effect of grain size on corrosion: a review, Corrosion 66 (7) (2010), 075005-075005-13.
[56] L. Liu, Y. Li, F. Wang, Electrochemical corrosion behavior of nanocrystalline materials—a review, J. Mater. Sci. Technol. 26 (1) (2010) 1–14.
[57] K. Sabet Bokati, C. Dehghanian, M. Babaei, Influence of near-surface severe plastic deformation of mild steel on the inhibition performance of sodium molybdate and 1H-benzotriazole in artificial sea water, J. Mater. Eng. Perform. 27 (2) (2018) 550–559, https://doi.org/10.1007/s11665-018-3130-3.
[58] R. Zhu, B. Lu, J. Luo, Y. Lu, Effect of cold work on surface reactivity and nano-hardness of alloy 800 in corroding environments, Appl. Surf. Sci. 270 (2013) 755–762.
[59] T. Wang, J. Yu, B. Dong, Surface nanocrystallization induced by shot peening and its effect on corrosion resistance of 1Cr18Ni9Ti stainless steel, Surf. Coat. Technol. 200 (16-17) (2006) 4777–4781.
[60] W. Zhao, et al., The effect of ultrasonic nanocrystal surface modification on low temperature nitriding of ultra-high strength steel, Surf. Coat. Technol. 375 (2019) 205–214, https://doi.org/10.1016/j.surfcoat.2019.07.006.
[61] Z. Wang, N. Tao, W. Tong, J. Lu, K. Lu, Diffusion of chromium in nanocrystalline iron produced by means of surface mechanical attrition treatment, Acta Mater. 51 (14) (2003) 4319–4329.
[62] L. Tan, X. Ren, K. Sridharan, T. Allen, Effect of shot-peening on the oxidation of alloy 800H exposed to supercritical water and cyclic oxidation, Corros. Sci. 50 (7) (2008) 2040–2046.
[63] C. Chen, C.J. Shang, D.Y. Li, A combination of Al diffusion and surface nanocrystallization of carbon steel for enhanced corrosion resistance, Philos. Mag. Lett. 89 (4) (2009) 231–240, https://doi.org/10.1080/09500830902722806.
[64] X. Ren, K. Sridharan, T.R. Allen, Effect of grain refinement on corrosion of ferritic-martensitic steels in supercritical water environment, Mater. Corros. 61 (9) (2010) 748–755, https://doi.org/10.1002/maco.200905446.
[65] S. Bahl, P. Shreyas, M. Trishul, S. Suwas, K. Chatterjee, Enhancing the mechanical and biological performance of a metallic biomaterial for orthopedic applications through changes in the surface oxide layer by nanocrystalline surface modification, Nanoscale 7 (17) (2015) 7704–7716.
[66] K. Selvam, P. Mandal, H.S. Grewal, H.S. Arora, Ultrasonic cavitation erosion-corrosion behavior of friction stir processed stainless steel, Ultrason. Sonochem. 44 (June) (2018) 331–339, https://doi.org/10.1016/j.ultsonch.2018.02.041.
[67] H.J. Grabke, Corrosion by carbonaceous gases, carburization and metal dusting, and methods of prevention, Mater. High Temp. 17 (4) (2000) 483–487.
[68] C. Hermse, H. Asteman, R. IJzerman, D. Jakobi, The influence of surface condition on the metal dusting behavior of cast and wrought chromia forming alloys, Mater. Corros. 64 (10) (2013) 856–865.
[69] H. Grabke, E. Müller-Lorenz, B. Eltester, M. Lucas, Formation of chromium rich oxide scales for protection against metal dusting, Mater. High Temp. 17 (2) (2000) 339–345.
[70] H.J. Grabke, E.M. Mueller-Lorenz, Occurrence and prevention of metal dusting on stainless steels. Corrosion 2001, NACE International, 2001.
[71] M. Hänsel, C. Boddington, D. Young, Internal oxidation and carburisation of heat-resistant alloys, Corros. Sci. 45 (5) (2003) 967–981.
[72] C.-Y. Lin, C.-H. Chang, W.-T. Tsai, Morphological and microstructural aspects of metal dusting on 304L stainless steel with different surface treatments, Oxid. Met. 62 (3) (2004) 153–174.
[73] C. Chun, T. Ramanarayanan, Metal dusting corrosion of austenitic 304 stainless steel, J. Electrochem. Soc. 152 (5) (2005) B169–B177.
[74] A. Vernouillet, A.V. Put, A. Pugliara, S. Doublet, D. Monceau, Metal dusting of Inconel 625 obtained by laser beam melting: effect of manufacturing process and hot isostatic pressure treatment, Corros. Sci. 174 (2020) 108820.
[75] P. Gunawardana, Carbon Formation Phenomena and the Initial Stage of Metal Dusting Corrosion–An Experimental Investigation, 2014.
[76] X. Guo, et al., Effects of metal dusting relevant exposures of alloy 601 surfaces on carbon formation and oxide development, Catal. Today (2020).
[77] A.C. Ferrari, D.M. Basko, Raman spectroscopy as a versatile tool for studying the properties of graphene, Nat. Nanotechnol. 8 (April (4)) (2013) 235–246, https://doi.org/10.1038/nnano.2013.46.
[78] I. Childres, L.A. Jauregui, W. Park, H. Cao, Y.P. Chen, Raman spectroscopy of graphene and related materials, New Dev. Photon Mater. Res. 1 (2013).
[79] X. Guo, P. Gunawardana, D. Chen, E. Vanhaecke, H. Venvik, J. Walmsley, Investigation of metal dusting corrosion process over UNS N08800 alloy. Corrosion 2017, NACE International, 2017.
[80] Y. Chen, Z. Liu, S.P. Ringer, Z. Tong, X. Cui, Y. Chen, Selective oxidation synthesis of MnCr2O4 spinel nanowires from commercial stainless steel foil, Cryst. Growth Des. 7 (11) (2007) 2279–2281.
[81] B.D. Hosterman, Raman Spectroscopic Study of Solid Solution Spinel Oxides, 2011.
[82] R. Farrow, P. Mattern, A. Nagelberg, Characterization of surface oxides by Raman spectroscopy, Appl. Phys. Lett. 36 (3) (1980) 212–214.
[83] D. Thierry, et al., In-situ Raman spectroscopy combined with x-ray photoelectron spectroscopy and nuclear microanalysis for studies of anodic corrosion film formation on Fe-Cr single crystals, J. Electrochem. Soc. 135 (2) (1988) 305–310.
[84] H. Liu, W. Chen, Coke formation and metal dusting of electroplated Ni3Al–CeO2-based coatings in CO–H2–H2O, Corros. Sci. 49 (11) (2007) 4134–4153.
[85] S. Persaud, S. Ramamurthy, A. Korinek, G. Botton, R. Newman, The influence of the high Fe and Cr contents of Alloy 800 on its inter-and intragranular oxidation tendency in 480° C hydrogenated steam, Corros. Sci. 106 (2016) 117–126.
[86] P.D.S. Gunawardana, T.T.M. Nguyen, J.C. Walmsley, H.J. Venvik, Initiation of metal dusting corrosion in conversion of natural gas to syngas studied under industrially relevant conditions, Ind. Eng. Chem. Res. 53 (5) (2013) 1794–1803.
[87] M. Gerland, C. Vernault, J. Mendez, Interaction of oxide layers with dislocations for an austenitic stainless steel, Mater. Sci. Eng. A 311 (1) (2001) 157–161.
[88] D. Baer, M. Merz, Differences in oxides on large-and small-grained 304 stainless steel, Metall. Trans. A 11 (12) (1980) 1973–1980.
[89] S. Persaud, S. Ramamurthy, R. Newman, Internal oxidation of alloy 690 in hydrogenated steam, Corros. Sci. 90 (2015) 606–613.
[90] B. Langelier, S. Persaud, R. Newman, G. Botton, An atom probe tomography study of internal oxidation processes in Alloy 600, Acta Mater. 109 (2016) 55–68.
[91] D.J. Young, High Temperature Oxidation and Corrosion of Metals, Elsevier, 2008.
[92] H. Grabke, I. Wolf, Carburization and oxidation, Mater. Sci. Eng. 87 (1987) 23–33.
[93] M. Harper, M. Ducasse, D. Young, Cyclic oxidation plus carburization of heat-resistant alloys, Corrosion 51 (3) (1995) 191–200.
[94] T.-C. Luan, R.E. Eckert, L.F. Albright, Gaseous pretreatment of high-alloy steels used in ethylene furnaces: pretreatment of Incoloy 800, Ind. Eng. Chem. Res. 42 (20) (2003) 4741–4747.